Engineering Fracture Mechanics 78 (2011) 1505–1513

Contents lists available at ScienceDirect

Engineering Fracture Mechanics

journal homepage: www.elsevier.com/locate/engfracmech

Nucleation and growth of domains near crack tips in single crystal ferroelectrics

Wenyuan Li, Chad M. Landis *

The University of Texas at Austin, Department of Aerospace Engineering and Engineering Mechanics, 210 East 24th Street, C0600, Austin, TX 78712-0235, United States

ARTICLE INFO

Article history:
Received 8 October 2010
Received in revised form 10 December 2010
Accepted 4 January 2011
Available online 8 January 2011

Keywords:
J-integral
Ferroelectrics
Phase-field modeling
Fracture
Domain nucleation and growth

ABSTRACT

The nucleation and growth of domains is investigated near a stationary crack tip in a single crystal of ferroelectric material. The phase-field approach, applying the material polarization as the order parameter, is used as the theoretical modeling framework and the finite element method is used for the numerical solution technique. The electromechanical form of the *J*-integral is appropriately modified to account for the polarization gradient energy terms, and analyzed to illustrate the amount of shielding, or lack thereof, due to domain switching at the crack tip. It is shown that the nucleation of domains near the crack tip due to applied electric field is affected by applied stress. However, the crack-tip energy release rate can change significantly between the instant of domain nucleation and the final equilibrium domain configuration. Implications of these results for ferroelectric single crystal fracture criteria are discussed.

1. Introduction

The phase-field modeling approach has been used successfully to study several different features of ferroelectric domain switching behavior including the structure of domain walls [1], switching of polycrystals and single crystals [2–4], switching in micro/nanostructures [5–10], the interactions of domain walls with charge defects and dislocations [11–14], and domain switching near crack tips [15–17]. The phase-field modeling approach allows for a detailed accounting of the electromechanical processes that occur during domain nucleation and growth. This modeling technique is useful in uncovering the coupled processes that occur during the fracture of ferroelectric materials. In order to obtain a better understanding of the energetics of fracture within the phase-field setting we modify the *J*-integral [18–20] to include the energies associated with the polarization order parameter, and demonstrate how the *J*-integral can be applied to determine the crack-tip energy release rate for common sets of electromechanical crack-face boundary conditions. We also present simulations of domain nucleation and the path-(in)dependence of the *J*-integral under equilibrium and non-equilibrium conditions.

2. Phase-field theory

Here we review the fundamental governing phase-field equations. For a detailed description of these equations the reader is referred to the work of Su and Landis [12]. Standard index notation is used with summation implied over repeated indices, the overdot represents the first derivative with respect to time, and, j represents partial differentiation with respect to the x_j coordinate direction.

* Corresponding author. Tel.: +1 512 471 4273; fax: +1 512 471 5500.
E-mail address: landis@mail.utexas.edu (C.M. Landis).

0013-7944/$ - see front matter © 2011 Elsevier Ltd. All rights reserved.
doi:10.1016/j.engfracmech.2011.01.002

The static equilibrium equations in any arbitrary volume V and its bounding surfaces S yield,

$$\sigma_{ji,j} + b_i = 0 \quad \text{in } V \tag{1}$$
$$\sigma_{ij} = \sigma_{ji} \quad \text{in } V \tag{2}$$
$$\sigma_{ji} n_j = t_i \quad \text{on } S \tag{3}$$

where σ_{ij} are the Cartesian components of the Cauchy stress, b_i the components of a body force per unit volume, n_i the components of a unit vector normal to a surface element, and t_i the tractions applied to a surface. Under the assumptions of linear kinematics, the strain components ε_{ij} are related to the displacements u_i as

$$\varepsilon_{ij} = \frac{1}{2}(u_{i,j} + u_{j,i}) \quad \text{in } V \tag{4}$$

The electrical quantities of electric field, E_i, electric potential, ϕ, electric displacement, D_i, volume charge density, q, and surface charge density, ω, are governed by the quasi-static forms of Maxwell's equations. Specifically,

$$D_{i,i} - q = 0 \quad \text{in } V \tag{5}$$
$$D_i n_i = -\omega \text{ on } S \tag{6}$$
$$E_i = -\phi_{,i} \tag{7}$$

within the phase-field modeling approach the free energy will also be required to depend on an order parameter and its gradient. Mathematically, the order parameter is used to describe the different variant types, i.e. the spontaneous states that are possible. For the case of ferroelectrics, the physically natural order parameter is the electrical polarization P_i. Note that the relationship between electric field, electric displacement and polarization in matter is given as

$$D_i = P_i + \kappa_0 E_i \tag{8}$$

Here κ_0 is the permittivity of free space. Given that the free energy is permitted to depend on an order parameter, a set of micro-forces are introduced that are work-conjugate to the order parameter and its gradient. The micro-force balance is written as,

$$\xi_{ji,j} + \pi_i + \gamma_i = 0 \tag{9}$$

where we have introduced a micro-force tensor ξ_{ji} such that $\xi_{ji} n_j \dot{P}_i$ represents the power density expended across surfaces, an *internal* micro-force vector π_i such that $\pi_i \dot{P}_i$ is the power density expended by the material internally (this micro-force accounts for dissipation in the material), and an external micro-force vector γ_i such that $\gamma_i \dot{P}_i$ is the power density expended by external sources. After the introduction of the Helmholtz free energy $\psi = \psi(\varepsilon_{ij}, D_i, P_i, P_{i,j})$, and an analysis of the second law of thermodynamics, the following constitutive relationships result.

$$\sigma_{ji} = \frac{\partial \psi}{\partial \varepsilon_{ij}}, \quad E_i = \frac{\partial \psi}{\partial D_i}, \quad \xi_{ji} = \frac{\partial \psi}{\partial P_{i,j}}, \quad \text{and } \pi_i = -\eta_i - \beta_{ij}\dot{P}_j \text{ with } \beta_{ij} \text{ positive definite, where } \eta_i \equiv \frac{\partial \psi}{\partial P_i} \tag{10}$$

The form of the Helmholtz free energy that is chosen to mimic the behavior of ferroelectric single crystals is,

$$\begin{aligned}\psi = {} & \frac{1}{2} a_{ijkl} P_{i,j} P_{k,l} + \frac{1}{2} \bar{a}_{ij} P_i P_j + \frac{1}{4} \bar{\bar{a}}_{ijkl} P_i P_j P_k P_l + \frac{1}{6} \bar{\bar{\bar{a}}}_{ijklmn} P_i P_j P_k P_l P_m P_n + \frac{1}{8} \bar{\bar{\bar{\bar{a}}}}_{ijklmnrs} P_i P_j P_k P_l P_m P_n P_r P_s + b_{ijkl} \varepsilon_{ij} P_k P_l \\ & + \frac{1}{2} c_{ijkl} \varepsilon_{ij} \varepsilon_{kl} + f_{ijklmn} \varepsilon_{ij} \varepsilon_{kl} P_m P_n + g_{ijklmn} \varepsilon_{ij} P_k P_l P_m P_n + \frac{1}{2\kappa_0} (D_i - P_i)(D_i - P_i)\end{aligned} \tag{11}$$

The specific values for the constants that are used to model barium titanate are listed in the Appendix. The representation of this free energy contains a few important material parameters to be used for the normalization of the results in this paper, including the spontaneous polarization P_0, the spontaneous strain ε_0, the critical electric field for homogeneous 180° switching E_0, the characteristic stress $\sigma_0 = E_0 P_0 / \varepsilon_0$, and the domain wall length scale l_0.

3. The *J*-integral

We now proceed to the specification of the J-integral (for two-dimensional crack problems) for materials described with this phase-field theory. J is given as,

$$J = \int_\Gamma (h n_1 - \sigma_{ji} n_j u_{i,1} + D_i n_i E_1 - \xi_{ji} n_j P_{i,1}) d\Gamma \tag{12}$$

Here we have introduced the electrical enthalpy h which can be related to the Helmholtz free energy through the Legendre transformation $h(\varepsilon_{ij}, P_i, P_{i,j}, E_i) = \psi - E_i D_i$. Note that through h the constitutive relationships become $\sigma_{ji} = \frac{\partial h}{\partial \varepsilon_{ij}}$, $D_i = -\frac{\partial h}{\partial E_i}$, $\xi_{ji} = \frac{\partial h}{\partial P_{i,j}}$, and $\eta_i = \frac{\partial h}{\partial P_i}$.

We first demonstrate that J is equal to zero around any closed contour not enclosing a singularity.

$$J = \int_\Gamma (hn_1 - \sigma_{ji}n_j u_{i,1} + D_i n_i E_1 - \xi_{ji}n_j P_{i,1})d\Gamma = \int_A (h_{,1} - \underbrace{\sigma_{ji,j}}_{-b_i} u_{i,1} - \sigma_{ji}u_{i,j1} + \underbrace{D_{i,i}}_{q} E_1 + D_i E_{i,1} - \underbrace{\xi_{ji,j}}_{\eta_i + \beta_{ij}\dot{P}_j} P_{i,1} - \xi_{ji}P_{i,j1})dA$$

$$= \int_A (h_{,1} - \sigma_{ji}u_{i,j1} + D_i E_{i,1} - \eta_i P_{i,1} - \xi_{ji}P_{i,j1})dA \quad \text{if } b_i = 0, \quad q = 0, \quad \text{and } \dot{P}_i = 0 \text{ in } A$$

$$= \int_A \left(\underbrace{\frac{\partial h}{\partial \varepsilon_{ij}}}_{\sigma_{ji}} \varepsilon_{ij,1} + \underbrace{\frac{\partial h}{\partial E_i}}_{-D_i} E_{i,1} + \underbrace{\frac{\partial h}{\partial P_i}}_{\eta_i} P_{i,1} + \underbrace{\frac{\partial h}{\partial P_{i,j}}}_{\xi_{ji}} P_{i,j1} - \underbrace{\sigma_{ji}u_{i,j1}}_{\sigma_{ji}\varepsilon_{ij,1}} + D_i E_{i,1} - \eta_i P_{i,1} - \xi_{ji}P_{i,j1} \right) dA = 0 \tag{13}$$

Note that this result only holds under the conditions where $b_i = 0$, $q = 0$, and $\dot{P}_i = 0$ in the area within the closed contour A. Most notably this result requires that the micro-force balance associated with the order parameter must be in equilibrium, and specifically the "viscous" term $\beta_{ij}\dot{P}_j$ must vanish.

Next, we recognize that the crack-tip energy release rate $\mathscr{G}$ is equal to the J-integral for an infinitesimally small contour about the crack tip. Proof of this fact follows similar argument due to Rice [20]. Then, by computing J about the contour illustrated in Fig. 1, it can be shown that,

$$\mathscr{G} = J_{\Gamma_{\text{tip}}} = J_\Gamma + J_{\Gamma_1} + J_{\Gamma_2} \tag{14}$$

$$J_\Gamma = \int_\Gamma (hn_1 - \sigma_{ji}n_j u_{i,1} + D_i n_i E_1 - \xi_{ji}n_j P_{i,1})d\Gamma \tag{15}$$

$$J_{\Gamma_1} = \int_{x_1^+}^0 (\sigma_{21}u_{1,1} + \sigma_{22}u_{2,1} - D_2 E_1)dx_1 \quad \text{assuming } \xi_{ji}n_j = 0 \text{ on the crack faces} \tag{16}$$

$$J_{\Gamma_2} = \int_{x_1^-}^0 (-\sigma_{21}u_{1,1} - \sigma_{22}u_{2,1} + D_2 E_1)dx_1 \text{ assuming } \xi_{ji}n_j = 0 \text{ on the crack faces} \tag{17}$$

The assumption of $\xi_{ji}n_j = 0$ is a reasonable assumption on any free surface, but this restriction is easily relaxed for other assumptions. The remaining crack-face boundary conditions are less well-defined. Two very popular sets of crack-face boundary conditions are the permeable and impermeable boundary conditions [21–24]. Both of these sets of boundary conditions assume that the crack faces are traction free. For the impermeable boundary conditions it is assumed that the normal component of the electric displacement is zero, and for the permeable boundary conditions it is assumed that both the electric potential and the normal component of the electric displacement are continuous across the crack. For the impermeable boundary conditions $J_{\Gamma_1} = J_{\Gamma_2} = 0$ and for the permeable boundary conditions $J_{\Gamma_1} + J_{\Gamma_2} = 0$ if $x_1^+ = x_1^- = x_1^\Gamma$. In either case the J-integral around any remote contour, with $x_1^+ = x_1^- = x_1^\Gamma$, is equal to the crack-tip energy release rate, $\mathscr{G} = J_\Gamma$.

The impermeable boundary conditions are generally too strong in situations where the single crystal has some initial polarization with a component normal to the crack faces. In such situations it is possible and perhaps likely that charge layers will reside on the crack faces to balance the normal component of the polarization. Hence, a modified form of the impermeable boundary conditions would allow for these charge layers such that $D_2^\pm = \omega_0$, where $\omega_0 = P_2^s$ is the surface charge density required to balance the initial spontaneous polarization in the material. For the sake of simplicity we will assume that this spontaneous polarization is homogeneous throughout the crystal (or at least on the crack faces), although more complicated distributions could also be envisioned and analyzed. We will also retain the traction free conditions. Under these circumstances we can show that,

$$J_{\Gamma_1} + J_{\Gamma_2} = \omega_0 \int_{x_1^+}^0 \frac{\partial \phi}{\partial x_1} dx_1 - \omega_0 \int_{x_1^-}^0 \frac{\partial \phi}{\partial x_1} dx_1 = -\omega_0 \left[\phi(x_1^+, 0) - \phi(x_1^-, 0) \right] \tag{18}$$

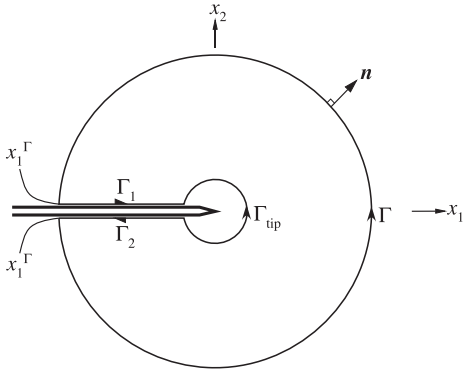

Fig. 1. The closed contour used to evaluate the crack-tip energy release rate.

Then, the crack-tip energy release rate is,

$$\mathscr{G} = J_\Gamma - \omega_0\left[\phi(x_1^+,0) - \phi(x_1^-,0)\right]. \tag{19}$$

In addition to these linear boundary conditions there have also been two sets of non-linear crack-face boundary conditions. The semi-permeable boundary conditions due to Hao and Shen [25–28], and the energetically consistent boundary conditions due to Landis [29–32]. Since it has been shown that the semi-permeable boundary conditions lead to a discrepancy between the total and crack-tip energy release rates [28,29], we will focus only on the energetically consistent boundary conditions here. The energetically consistent boundary conditions postulate that the medium within the crack gap can be described by an electrical enthalpy $h_c = h_c(E_c)$, where E_c is the electric field within the crack gap. This approximation assumes that the crack gap can be treated as a one-dimensional capacitor where the tangential components of the electric field are neglected. Then E_c is given as,

$$E_c = -\frac{\Delta\phi}{\Delta u_2} \tag{20}$$

where $\Delta u_2 = u_2^+ - u_2^-$ is the crack opening displacement and $\Delta\phi = \phi^+ - \phi^-$ is the electric potential jump across the crack faces. The electric displacement and the *stress* within the crack gap are derived from the crack gap electrical enthalpy as,

$$D_c = -\frac{dh_c}{dE_c} \text{ and } \sigma_c = h_c + E_c D_c \tag{21}$$

Allowing for the initial charge layers on the crack faces the energetically consistent crack-face boundary conditions become,

$$\sigma_{21}^{\pm} = 0, \quad \sigma_{22}^{\pm} = \sigma_c, \quad \text{and} \quad D_2^{\pm} = \omega_0 + D_c$$

Then, using $x_1^+ = x_1^- = x_1^\Gamma$ the analysis of the crack-face J paths follows as,

$$\begin{aligned}
J_{\Gamma_1} + J_{\Gamma_1} &= \int_{x_1^\Gamma}^{0}\left[\sigma_c\Delta u_{2,1} + (\omega_0 + D_c)\Delta\phi_{,1}\right]dx_1 = \int_{x_1^\Gamma}^{0}\left[(h_c + E_c D_c)\Delta u_{2,1} + (\omega_0 + D_c)\Delta\phi_{,1}\right]dx_1 \\
&= \int_{x_1^\Gamma}^{0}\left[\left(h_c - \frac{\Delta\phi}{\Delta u_2}D_c\right)\Delta u_{2,1} + (\omega_0 + D_c)\Delta\phi_{,1}\right]dx_1 \\
&= \int_{x_1^\Gamma}^{0}\left[(h_c\Delta u_2 - \Delta\phi D_c)_{,1} - h_{c,1}\Delta u_2 + \Delta\phi D_{c,1} + \Delta\phi_{,1}D_c - \frac{\Delta\phi}{\Delta u_2}D_c\Delta u_{2,1} + (\omega_0\Delta\phi + D_c\Delta\phi)_{,1} - D_{c,1}\Delta\phi\right]dx_1 \\
&= \int_{x_1^\Gamma}^{0}\left[(h_c\Delta u_2 + \omega_0\Delta\phi)_{,1} - \frac{dh_c}{dE_c}E_{c,1}\Delta u_2 + \Delta\phi D_{c,1} + \Delta\phi_{,1}D_c + E_c D_c\Delta u_{2,1} - D_{c,1}\Delta\phi\right]dx_1 \\
&= \int_{x_1^\Gamma}^{0}\left[(h_c\Delta u_2 + \omega_0\Delta\phi)_{,1} - D_c\left(\frac{\Delta\phi_{,1}}{\Delta u_2} - \frac{\Delta\phi\Delta u_{2,1}}{(\Delta u_2)^2}\right)\Delta u_2 + \Delta\phi D_{c,1} + \Delta\phi_{,1}D_c + E_c D_c\Delta u_{2,1} - D_{c,1}\Delta\phi\right]dx_1 \\
&= \int_{x_1^\Gamma}^{0}(h_c\Delta u_2 + \omega_0\Delta\phi)_{,1}dx_1 = -h_c^\Gamma\Delta u_2^\Gamma - \omega_0\Delta\phi^\Gamma
\end{aligned}$$

Hence, the crack-tip energy release rate is,

$$\mathscr{G} = J_\Gamma - h_c^\Gamma\Delta u_2^\Gamma - \omega_0\Delta\phi^\Gamma. \tag{22}$$

We note that there are limiting representations of h_c that can be used to reproduce both the impermeable and permeable boundary conditions. Notably, when the dielectric breakdown strength of the crack gap medium is small (rigorously in the limit as this strength goes to zero) the permeable boundary conditions are recovered, giving a possible physical mechanism for this model of the crack-face boundary conditions.

4. Simulation results

In this section we present simulation results to demonstrate under what conditions a remote J path can be used to determine the crack-tip energy release rate. The governing equations were solved using the finite element method described in Ref. [12]. We first study two-dimensional square geometries with the length of the side of the square equal to $60l_0$ or $200l_0$ and the crack length equal to $30l_0$ or $100l_0$. The characteristic thickness of a domain wall within the theory is $2l_0$. The material properties used are characteristic of barium titanate and are listed in the Appendix. In all cases we use the generalized impermeable boundary conditions on the crack faces such that the crack faces are traction free and there is a fixed surface charge density on the crack faces that exactly balances the normal component of the initial spontaneous polarization.

The first set of simulations is for a material with initial spontaneous polarization P_0 normal to the crack faces in a $200l_0 \times 200l_0$ domain. The entire boundary of the square region is traction free, and the left and right sides of the region have no surface charge density. The top and bottom surfaces have an applied surface charge density of $\omega^{\pm} = \mp(P_0 - \omega_A)$. Note that

when the surface charge increment ω_A is equal to zero, the stresses and electric fields in the sample are also equal to zero. The normalized rates of charge loading investigated were $\beta\dot{\omega}_A/E_0 = 0, 0.1, and 1$, with $\beta\dot{\omega}_A/E_0 = 0$ corresponding to equilibrium calculations. The parameter E_0 is the characteristic level of electric field required to cause homogeneous 180° switching of a spontaneously polarized sample. Fig. 2 illustrates the path-dependence of the apparent energy release rate computed from $\mathscr{G}_\Gamma = J_\Gamma - \omega_0[\phi(x_1^+,0) - \phi(x_1^-,0)]$ for a small charge load level $\omega_A/P_0 = 0.05$ for the three loading rates. The far-field value of $\mathscr{G}_\Gamma$ is $\mathscr{G}_{95}/E_0P_0l_0 = -1.8$, -3.5 and -18.2 for $\beta\dot{\omega}_A/E_0 = 0, 0.1$, and 1 respectively. Note that for the equilibrium case the calculation of $\mathscr{G}_\Gamma$ is path-independent and a valid result for the crack-tip energy release rate is obtained for any path. For the two non-equilibrium cases the calculation is not path-independent and cannot be interpreted as the crack-tip energy release rate except in the limit as $x_1^\Gamma \to 0$. Finally, this path-dependent behavior cannot be interpreted as shielding due to domain switching, since no domain switching has occurred in these calculations. The path-dependence is due to the dissipative behavior of the term $\beta\dot{P}_i$ in the micro-force balance.

Generating domain switching zones in these calculations for the equilibrium cases with $\beta\dot{\omega}_A/E_0 = 0$ is not a trivial task. For the $200l_0 \times 200l_0$ region it is not possible to find equilibrium solutions for $\omega_A/P_0 > 0.08$ by simply incrementing the electrical loading with $\beta = 0$. This suggests an instability in the solution which is due to a new domain structure nucleating at the crack tip. Such conditions for domain nucleation at a crack tip can be studied under small-scale-switching conditions wherein the material region near the crack tip experiencing loadings of sufficient magnitude to cause considerable non-linear response is small in comparison to any other length scales associated with the specimen like crack size or ligament length. For such situations the electromechanical fields in a so-called *K*-annulus will be dominated by the linear piezoelectric K_I–K_D fields. The K_I–K_D fields are generated with the Stroh formalism and the mechanical displacements and electric potential associated with these fields are applied to the outer boundary of the $200l_0 \times 200l_0$ region. The mode I stress intensity factor, K_I, and the electric displacement intensity factor, K_D, are increased proportionally until an instability in the solution is found. This instability is associated with the nucleation of a new domain from the crack tip. The growth of such a domain will be presented next. Fig. 3 shows a schematic of the crack loaded by the K_I–K_D fields and then a plot of the critical combinations of K_I and K_D required to nucleate a new domain in a material with initial spontaneous polarization perpendicular to the crack faces. The generalized impermeable crack-face boundary conditions are applied in these simulations. First note that the orientation of range of the K_D fields plotted in Fig. 3 is such that the initial spontaneous polarization in the sample tends to be reversed. Also note that the intensity factors are normalized by material specific properties including the domain wall length scale l_0. The results displayed in Fig. 3 show that the mechanical loading plays very little role in the nucleation of a new domain from the crack tip for these material properties. These results are in qualitative theories based upon energetic considerations which postulate that 90° switching occurs when the work due to the applied stresses and electric fields on a switching process attain a critical level. Roughly, without accounting for all of the details of the near-tip fields, such an approximation yields,

$$\frac{K_I}{\sigma_0\sqrt{l_0}} + \frac{K_D}{P_0\sqrt{l_0}}\frac{P_0}{\kappa E_0} = \text{constant}. \tag{23}$$

The dashed line in Fig. 3 shows this approximation when the constant is fit to the point when $K_I = 0$. When considering (23), note that E_0 is the critical field for *homogeneous* 180° switching, not the field required to move existing domain walls which is considerably smaller.

Next, the growth of a new domain from a crack tip during purely electrical loading is simulated. To generate the solution for a final equilibrium domain configuration, the domain was nucleated at the crack tip and then allowed to evolve with a non-zero polarization viscosity term. The loading is applied by first ramping up a uniform charge load on the top and bottom surfaces with a charging rate of $\beta\dot{\omega}_A/E_0 = 0.1$ to a total charge of $\omega_A/P_0 = 0.12$ in a $60l_0 \times 60l_0$ domain. The charge was then fixed at $\omega_A/P_0 = 0.12$ and the domain structure was allowed to evolve until the solution was sufficiently close to the

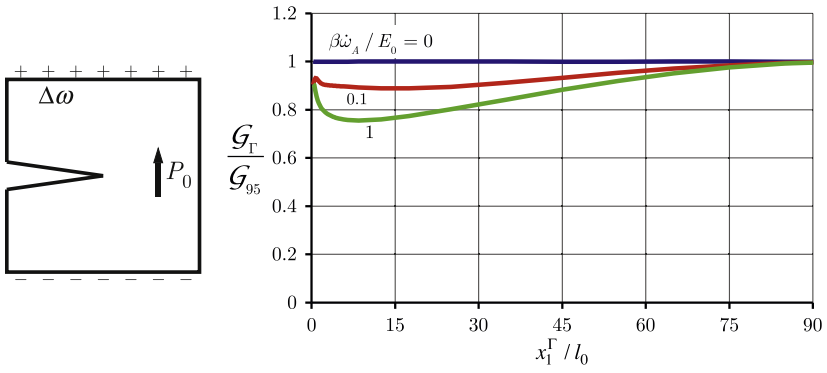

Fig. 2. The apparent crack-tip energy release rate computed using $\mathscr{G}_\Gamma = J_\Gamma - \omega_0[\phi(x_1^+,0) - \phi(x_1^-,0)]$ at a charge loading level of $\omega_A/P_0 = 0.05$. The *J*-contour used to compute $\mathscr{G}_\Gamma$ is a square contour with sides of length $2x_1^\Gamma$.

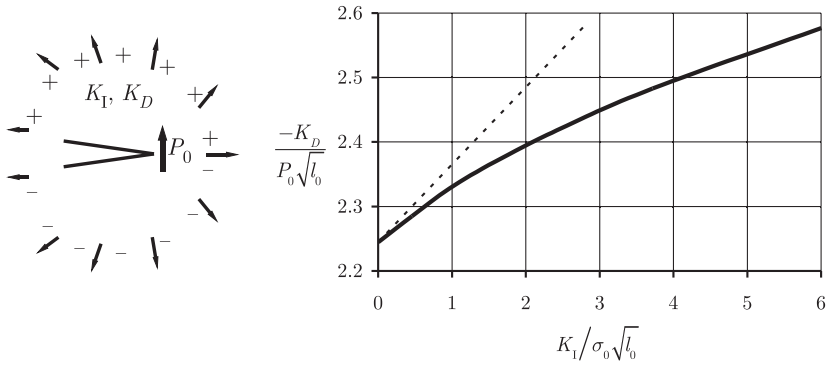

Fig. 3. A semi-infinite crack loaded by a combination of electrical and mechanical loads characterized by the mode I stress intensity factor, K_I, and the electric displacement intensity factor, K_D. The graph plots the critical combination of intensity factors required to nucleate a new domain at the crack tip. The solid line is calculated from the full model equations and the dashed line is from Eq. (23) with the constant fit to the point at $K_I = 0$. Note that the mechanical stress intensity has little effect on the nucleation process for this configuration of crack face and spontaneous polarization orientation.

equilibrium configuration, at which point the polarization viscosity term was set to $\beta = 0$ to find the true equilibrium solution. Thereafter additional charge is applied to the surface to a final value of $\omega_A/P_0 = 0.2$ and finally the charge is removed from the surface to return to the initial uncharged state. Note that in order to ensure accuracy of the computations at least five finite element nodes span any domain wall, and the path-independence of the J-integral is verified for all cases of equilibrium. If the mesh is too coarse then mesh-pinning of the domains occurs and significant but artificial path-dependence appears at equilibrium in the J-integral. Fig. 4 shows contour plots of the y component of the polarization distributions at four different times in the domain evolution. Fig. 4 shows that the 90° domain needle is nucleated at the crack tip and propagates through the entire domain until it reaches the charged boundary.

This non-equilibrium propagation of the domain supports the hypothesis that an instability in the equilibrium solution exists at the domain nucleation threshold. Additionally, the equilibrium configurations just prior to the domain nucleation with no domain and that shown in Fig. 4b both occur at a charge loading level of $\omega_A/P_0 = 0.12$, and are sufficiently distinct from one another. This unstable growth of domains is in contrast to domain switching zones predicted using phenomenological constitutive laws [33–38]. The explanation for the discrepancy is that these phase-field simulations assume a defect-free material. In such a material domain walls do not become pinned and are free to move at vanishingly small levels of electromechanical driving force [12].

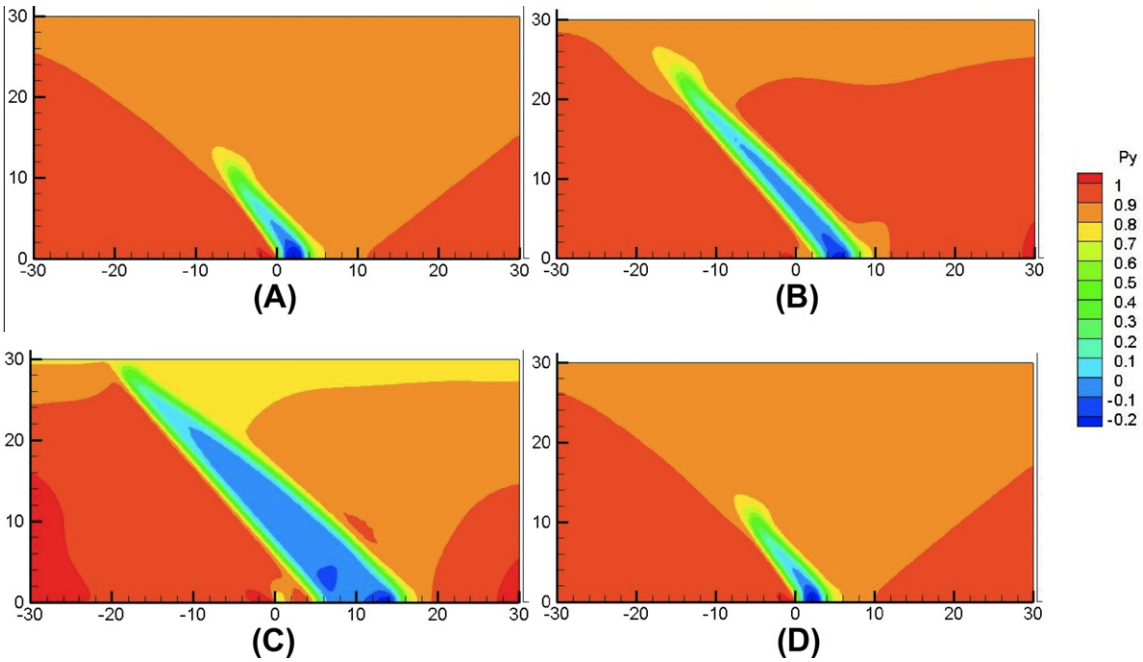

Fig. 4. Contour plots of the y component of the polarization normalized by P_0 in the vicinity of the crack tip for (A) $\omega_A/P_0 = 0.12$ during the non-equilibrium evolution of the domain, (B) $\omega_A/P_0 = 0.12$ at the final equilibrium state for the domain, (C) equilibrium at $\omega_A/P_0 = 0.2$, and (D) equilibrium at $\omega_A/P_0 = 0.11$. Only the upper half of the region is displayed. The x and y distances are normalized distances x/l_0 and y/l_0, and the polarization scale is normalized by the spontaneous polarization P_0.

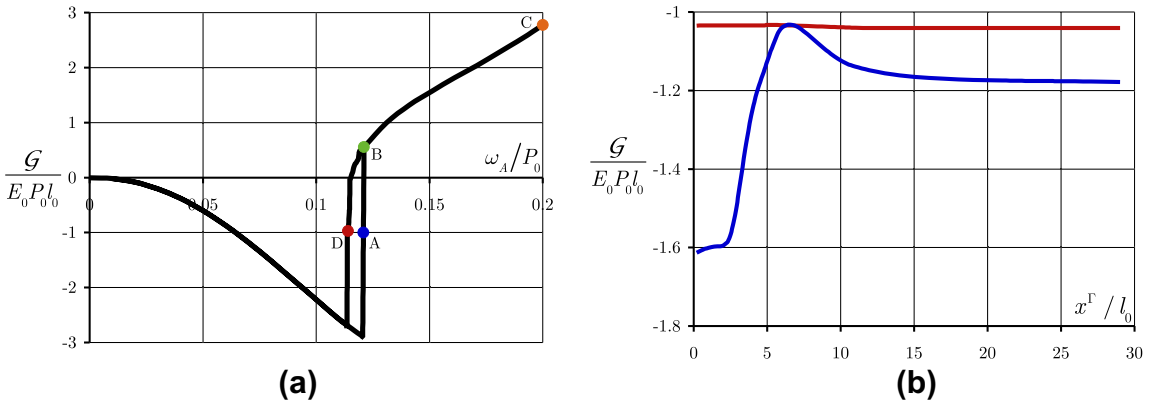

Fig. 5. (a) The crack-tip energy release rate as a function of the applied charge. Points A–D correspond to the domain structures illustrated in Fig. 4A–D respectively. (b) The apparent energy release rate as calculated by Eq. (18) for domain structures A (blue, non-equilibrium) and D (red, equilibrium). (For interpretation of the references to color in this figure legend, the reader is referred to the web version of this article.)

Next, results for the apparent crack-tip energy release rate calculation are presented. Fig. 5a plots the apparent energy release rate as a function of the applied charge loading for the sample. Note that points A–D on Fig. 5a correspond to the domain structures illustrated in Fig. 4A–D respectively. Initially, as the charge is applied the energy release rate is negative and approximately quadratic in the applied charge. These features of the energy release rate are in accord with linear piezoelectric fracture mechanics solutions [22–24].

Furthermore, prior to the nucleation of the new domain, the solutions are carried out at equilibrium and the energy release rate calculation is path-independent. At the charge load level of $\omega_A/P_0 = 0.12$, nucleation of the new domain occurs, and at this point the crack-tip energy release rate is approximately $\mathcal{G} = -3E_0P_0l_0$. The charge is held fixed at this point and as the new domain grows the energy release rate increases from $\mathcal{G} = -3E_0P_0l_0$ to $\mathcal{G} = 0.5E_0P_0l_0$. Note that the domain evolution at $\omega_A/P_0 = 0.12$ is a non-equilibrium process during which the apparent energy release rate calculation is path-dependent. Specifically, path-dependence of the apparent energy release rate calculation for domain structure A is plotted as the blue curve in Fig. 5b. Domain structure B is again an equilibrium configuration and the energy release rate calculation is path-independent. After domain structure B stabilizes, additional charge is applied and the domain structure is allowed to evolve at equilibrium to domain structure C. During this loading process the energy release rate increases in an approximately linear fashion. Upon reaching structure C the applied charge is removed and the domain structures and the energy release rate "unload" along their original loading paths to structure B. At this point the unloading path diverges from the original loading path and a hysteresis appears in the energy release rate versus applied charge response. Domain structure D is arrived at during the equilibrium unloading process and the energy release rate calculation is path-independent as shown by the red curve in Fig. 5b. Further unloading of the charge causes the domain to vanish and the original negative quadratic branch of the energy release rate response is followed.

The most interesting aspect of this simulation is the departure from the results of linear piezoelectric fracture mechanics. Specifically, this calculation is the first that we are aware of that predicts that the crack-tip energy release rate can be positive under purely electrical loading for impermeable crack-face boundary conditions. Furthermore, the calculation shows that an existing domain structure near the crack tip can cause a qualitatively different behavior for the energy release rate, positive and increasing with applied charge, from what is expected in linear piezoelectricity, negative and decreasing with applied charge. Since the domain structure introduces spatial dependence in the material properties its effect on the energy release rate is to some degree connected with the results generated by Oates [39]. Oates found that by introducing a heterogeneity near the crack and using the semi-permeable crack-face boundary conditions of Hao and Shen [25], a positive crack-tip energy release rate could be generated by purely electrical loading when the heterogeneity is close the crack tip. In the work presented here the domain is a heterogeneity and it is located at the crack tip. We do note that *large scale switching* does occur in this simulation and so a direct comparison to linear piezoelectric fracture mechanics concepts is tenuous. However, these simulations demonstrate the effects that near tip domain structures can have on the fracture process in ferroelectric crystals. Specifically, the negative contribution of the energy release rate from applied electric fields may in fact be positive for certain domain structures near crack tips. Hence, the modeling of crack tip domain structures and large scale domain switching behavior in fracture specimens may be a key to understanding the plethora of seemingly disparate experimental observations on electromechanical fracture of ferroelectrics [40–42]. Kuna [43] has recently provided an excellent review of these issues.

5. Discussion

In this paper a method for evaluating the crack-tip energy release rate using the *J*-integral within the phase-field modeling framework for ferroelectric domain evolution has been presented. Calculations were presented to investigate the

path-dependence of the method under both equilibrium and non-equilibrium conditions. The calculations indicate that only true equilibrium states exhibit path-independence, and that domain structures near crack tips may be responsible for allowing positive energy release rates during purely electrical loading.

Acknowledgements

This work has been supported by the Army Research Office Contract #W911NF-07-1-0495 and NSF Grant DMR-0909139.

Appendix A

Eq. (11) presented the general form of the Helmholtz free energy used in this paper. For a coordinate system aligned with the $\langle 1\,0\,0\rangle$ directions, the specific form used to fit the dielectric, piezoelectric and elastic properties of ferroelectric single crystals that undergo a cubic to tetragonal phase transformation is given in Eq. (A1).

$$\begin{aligned}\psi = {} & \frac{a_0}{2}\left(P_{1,1}^2+P_{2,2}^2+P_{3,3}^2+P_{1,2}^2+P_{2,1}^2+P_{1,3}^2+P_{3,1}^2+P_{2,3}^2+P_{3,2}^2\right)+\frac{a_1}{2}\left(P_1^2+P_2^2+P_3^2\right)+\frac{a_2}{4}\left(P_1^4+P_2^4+P_3^4\right)\\
& +\frac{a_3}{2}\left(P_1^2P_2^2+P_2^2P_3^2+P_1^2P_3^2\right)+\frac{a_4}{6}\left(P_1^6+P_2^6+P_3^6\right)+a_6\left(P_1^4\left(P_2^2+P_3^2\right)+P_2^4\left(P_1^2+P_3^2\right)+P_3^4\left(P_1^2+P_2^2\right)\right)\\
& +\frac{a_5}{4}\left(P_1^4P_2^4+P_2^4P_3^4+P_1^4P_3^4\right)-\frac{b_1}{2}\left(\varepsilon_{11}P_1^2+\varepsilon_{22}P_2^2+\varepsilon_{33}P_3^2\right)-\frac{b_2}{2}\left((\varepsilon_{22}+\varepsilon_{33})P_1^2+(\varepsilon_{11}+\varepsilon_{33})P_2^2+(\varepsilon_{11}+\varepsilon_{22})P_3^2\right)\\
& -b_3((\varepsilon_{12}+\varepsilon_{21})P_1P_2+(\varepsilon_{13}+\varepsilon_{31})P_1P_3+(\varepsilon_{23}+\varepsilon_{32})P_2P_3)+\frac{c_1}{2}\left(\varepsilon_{11}^2+\varepsilon_{22}^2+\varepsilon_{33}^2\right)+c_2(\varepsilon_{11}\varepsilon_{22}+\varepsilon_{11}\varepsilon_{33}+\varepsilon_{22}\varepsilon_{33})\\
& +\frac{c_3}{2}((\varepsilon_{12}+\varepsilon_{21})^2+(\varepsilon_{13}+\varepsilon_{31})^2+(\varepsilon_{23}+\varepsilon_{32})^2)\\
& +\left(\frac{f_1}{2}\varepsilon_{11}^2+\frac{f_2}{2}\left(\varepsilon_{22}^2+\varepsilon_{33}^2\right)+f_3(\varepsilon_{11}\varepsilon_{22}+\varepsilon_{11}\varepsilon_{33})+f_4\varepsilon_{22}\varepsilon_{33}+\frac{f_5}{2}((\varepsilon_{12}+\varepsilon_{21})^2+(\varepsilon_{13}+\varepsilon_{31})^2)+\frac{f_6}{2}(\varepsilon_{23}+\varepsilon_{32})^2\right)P_1^2\\
& +\left(\frac{f_1}{2}\varepsilon_{22}^2+\frac{f_2}{2}\left(\varepsilon_{11}^2+\varepsilon_{33}^2\right)+f_3(\varepsilon_{11}\varepsilon_{22}+\varepsilon_{22}\varepsilon_{33})+f_4\varepsilon_{11}\varepsilon_{33}+\frac{f_5}{2}((\varepsilon_{12}+\varepsilon_{21})^2+(\varepsilon_{23}+\varepsilon_{32})^2)+\frac{f_6}{2}(\varepsilon_{13}+\varepsilon_{31})^2\right)P_2^2\\
& +\left(\frac{f_1}{2}\varepsilon_{33}^2+\frac{f_2}{2}\left(\varepsilon_{11}^2+\varepsilon_{22}^2\right)+f_3(\varepsilon_{11}\varepsilon_{33}+\varepsilon_{22}\varepsilon_{33})+f_4\varepsilon_{11}\varepsilon_{22}+\frac{f_5}{2}((\varepsilon_{13}+\varepsilon_{31})^2+(\varepsilon_{23}+\varepsilon_{32})^2)+\frac{f_6}{2}(\varepsilon_{12}+\varepsilon 21)^2\right)P_3^2\\
& +\left(\frac{g_1}{4}\varepsilon_{11}+\frac{g_2}{4}(\varepsilon_{22}+\varepsilon_{33})\right)P_1^4+\left(\frac{g_1}{4}\varepsilon_{22}+\frac{g_2}{4}(\varepsilon_{11}+\varepsilon_{33})\right)P_2^4+\left(\frac{g_1}{4}\varepsilon_{33}+\frac{g_2}{4}(\varepsilon_{11}+\varepsilon_{22})\right)P_3^4+\frac{g_3}{4}(\varepsilon_{12}\\
& +\varepsilon_{21})\left(P_1P_2^3+P_2P_1^3\right)+\frac{g_3}{4}(\varepsilon_{13}+\varepsilon_{31})\left(P_1P_3^3+P_3P_1^3\right)+\frac{g_3}{4}(\varepsilon_{23}+\varepsilon_{32})\left(P_2P_3^3+P_3P_2^3\right)+\frac{1}{2\kappa_0}((D_1-P_1)^2+(D_2\\
& -P_2)^2+(D_3-P_3)^2)\end{aligned}\tag{A1}$$

In the equation above $\kappa_0 = 8.854\times10^{-12}$ V m/C, and

$$\begin{aligned}
&a_1=-0.668325E_0/P_0,\quad a_2=-3.80653E_0/P_0^3,\quad a_3=0.78922E_0/P_0^3\\
&a_4=12.4421E_0/P_0^5,\quad a_5=368E_0/P_0^7,\quad a_6=0.134226E_0/P_0^5\\
&b_1=2.54138E_0/\varepsilon_0P_0,\quad b_2=1.74267E_0/\varepsilon_0P_0,\quad b_3=0.399353E_0/\varepsilon_0P_0\\
&c_1=2.04999\sigma_0/\varepsilon_0,\quad c_2=0.971673\sigma_0/\varepsilon_0,\quad c_3=1.27976\sigma_0/\varepsilon_0\\
&f_1=0.663581E_0/\varepsilon_0^2P_0,\quad f_2=0.841326E_0/\varepsilon_0^2P_0,\quad f_3=-0.170635E_0/\varepsilon_0^2P_0\\
&f_4=0.687281E_0/\varepsilon_0^2P_0,\quad f_5=0.106647E_0/\varepsilon_0^2P_0,\quad f_6=0.213294E_0/\varepsilon_0^2P_0\\
&g_1=-3.66149E_0/\varepsilon_0P_0^3,\quad g_2=6.27423E_0/\varepsilon_0P_0^3,\quad g_3=-1.21644E_0/\varepsilon_0P_0^3
\end{aligned}$$

where $\sigma_0 = E_0P_0/\varepsilon_0 = 692\times10^6$ N/m^2. In addition, $P_0 = 0.26$ C/m^2, $\varepsilon_0 = 0.0082$ and $E_0 = 2.182\times10^7$ V/m correspond to properties of monodomain single crystal barium titanate at room temperature.

The parameter a_0 appearing in Eq. (A1) determines the domain wall thickness. If $a_0 = 1\times10^{-10}$V m^3/C then $l_0 = 1$ nm, and therefore the 180° domain wall has thickness equal to 2 nm which is in general agreement with experimental observations [44].

References

[1] Cao W, Cross LE. Theory of tetragonal twin structures in ferroelectric perovskites with a first-order phase transition. Phys Rev B 1991;44:5–12.
[2] Choudhury S, Li YL, Krill CE, Chen LQ. Phase-field simulation of polarization switching and domain evolution in ferroelectric polycrystals. Acta Mater 2005;53:5313–21.
[3] Zhang W, Bhattacharya K. A computational model of ferroelectric domains. Part I: model formulation and domain switching. Acta Mater 2005;53:185–98.
[4] Schrade D, Müller R, Gross D. Domain evolution in ferroelectric materials: a continuum phase field model and finite element implementation. Comput Methods Appl Mech Engng 2007;196:4365–74.

[5] Munch I, Huber JE. A hexadomain vortex in tetragonal ferroelectrics. Appl Phys Lett 2009;95:022913.
[6] Wang J, Kamlah M. Intrinsic switching of polarization vortex in ferroelectric nanotubes. Phys Rev B 2009;80:012101.
[7] Zuo YA, Wang J, Kamlah M. Effect of surface charges on the polarization distribution in ferroelectric nanotubes. Int J Mater Res 101:492-497.
[8] Gruverman A, Cross JS, Oates WS. Peculiar effect of mechanical stress on polarization stability in micrometer-scale ferroelectrics. Appl Phys Lett 2008;93:242902.
[9] Kontsos A, Landis CM. Phase-field modeling of domain structure energetics and evolution in ferroelectric thin films. J Appl Mech 2010;77:041014.
[10] Zhang YH, Li JY, Fang DN. Size dependent domain configuration and electric field driven evolution in ultrathin ferroelectric films: a phase field investigation. J Appl Phys 2010;107:034107.
[11] Xiao Y, Shenoy VB, Bhattacharya K. Depletion layers and domain walls in semiconducting ferroelectric thin films. Phys Rev Lett 2005;95:247603.
[12] Su Y, Landis CM. Continuum thermodynamics of ferroelectric domain evolution: theory, finite element implementation and application to domain wall pinning. J Mech Phys Solids 2007;55:280–305.
[13] Kontsos A, Landis CM. Computational modeling of domain wall interactions with dislocations in ferroelectric crystals. Int J Solids Struct 2009;46:1491–8.
[14] Zhang YH, Li JY, Fang DN. Oxygen-vacancy-induced memory effect and large recoverable strain in a barium titanate single crystal. Phys Rev B 2010;82:064103.
[15] Song YC, Soh AK, Ni Y. Phase field simulation of crack tip domain switching in ferroelectrics. J Phys D Appl Phys 2007;40:1175–82.
[16] Müller R, Gross D, Schrade D, Xu BX. Phase field simulation of domain structures in ferroelectric materials within the context of inhomogeneity evolution. Int J Fract 2007;147:173–80.
[17] Wang J, Kamlah M. Three-dimensional finite element modeling of polarization switching in a ferroelectric single domain with an impermeable notch. Smart Mater Struct 2009;18:104008.
[18] Eshelby JD. The energy momentum tensor in continuum mechanics. In: Kanninen MF et al., editors. Inelastic behavior of solids. New York: McGraw-Hill; 1970.
[19] Rice JR. A path independent integral and approximate analysis of strain concentration by notches and cracks. J Appl Mech 1968;35:379–86.
[20] Rice JR. Mathematical analysis in the mechanics of fracture. In: Liebowitz H, editor. Fracture: an advanced treatise, vol. II. New York: Academic Press; 1968. p. 191–311.
[21] Parton VZ. A fracture mechanics of piezoelectric materials. Acta Astronaut 1976;3:671–83.
[22] Sosa HA. On the fracture mechanics of piezoelectric solids. Int J Solids Struct 1992;29:2613–22.
[23] Pak YE. Linear electro-elastic fracture mechanics of piezoelectric materials. Int J Fract 1992;54:79–100.
[24] Suo Z, Kuo CM, Barnett DM, Willis JR. Fracture mechanics for piezoelectric solids. J Mech Phys Solids 1992;40:739–65.
[25] Hao TH, Shen ZY. A new electric boundary condition of electric fracture mechanics and its application. Engng Fract Mech 1994;47:793–802.
[26] Dunn ML. The effects of crack face boundary conditions on the fracture mechanics of piezoelectric solids. Engng Fract Mech 1994;48:25–39.
[27] McMeeking RM. Crack tip energy release rate for a piezoelectric compact tension specimen. Engng Fract Mech 1999;64:217–44.
[28] McMeeking RM. The energy release rate for a Griffith crack in a piezoelectric material. Engng Fract Mech 2004;71:1169–83.
[29] Landis CM. Energetically consistent boundary conditions for electromechanical fracture. Int J Solids Struct 2004;41:6291–315.
[30] Li W, McMeeking RM, Landis CM. On the crack face boundary conditions in electromechanical fracture and an experimental protocol for determining energy release rates. Eur J Mech A/Solid 2008;27:285–301.
[31] Motola Y, Banks-Sills L. M-integral for calculating intensity factors of cracked piezoelectric materials using the exact boundary conditions. J Appl Mech 2009;76:011004.
[32] Motola Y, Banks-Sills L, Fourman V. On fracture testing of piezoelectric ceramics. Int J Fract 2009;159:167–90.
[33] Landis CM. Fully coupled, multi-axial, symmetric constitutive laws for polycrystalline ferroelectric ceramics. J Mech Phys Solids 2002;50:127–52.
[34] Landis CM. On the strain saturation conditions for polycrystalline ferroelastic materials. J Appl Mech 2003;70:470–8.
[35] Landis CM, Wang J, Sheng J. Micro-electromechanical determination of the possible remanent strain and polarization states in polycrystalline ferroelectrics and the implications for phenomenological constitutive theories. J Intell Mater Syst Struct 2004;15:513–25.
[36] Yang W, Zhu T. Switch-toughening of ferroelectrics under electric field. J Mech Phys Solids 1998;46:291–311.
[37] Wang J, Landis CM. On the fracture toughness of ferroelectric ceramics with electric field applied parallel to the crack front. Acta Mater 2004;52:3435–46.
[38] Wang J, Landis CM. Effects of in-plane electric fields on the toughening behavior of ferroelectric ceramics. J Mech Mater Struct 2006;1:1075–95.
[39] Oates WS. Heterogeneity influence on electric field induced piezoelectric microfracture. J Intell Mater Syst Struct 2005;16:733–41.
[40] Park SB, Sun CT. Effect of electric field on fracture of piezoelectric ceramics. Int J Fract 1995;70:203–16.
[41] Lynch CS, Yang W, Collier L, Suo Z, McMeeking RM. Electric field induced cracking in ferroelectric ceramics. Ferroelectrics 1995;166:11–30.
[42] Schnieder GA, Heyer V. Influence of the electric field on Vickers indentation crack growth in $BaTiO_3$. J Eur Ceram Soc 1999;19:1299–306.
[43] Kuna M. Fracture mechanics of piezoelectric materials – where are we right now? Engng Fract Mech 2010;77:309–26.
[44] Zhang X, Hashimoto T, Joy DC. Electron holographic study of ferroelectric domain walls. Appl Phys Lett 1992;60:784–6.